Intrinsic Nonlinear Hall Effect in Antiferromagnetic Tetragonal CuMnAs

Chong Wang,[1] Yang Gao,[2,3,*] and Di Xiao[1,†]

[1]Department of Physics, Carnegie Mellon University, Pittsburgh, Pennsylvania 15213, USA
[2]ICQD, Hefei National Laboratory for Physical Sciences at Microscale, University of Science and Technology of China, Hefei, Anhui 230026, China
[3]Department of Physics, University of Science and Technology of China, Hefei, Anhui 230026, China

(Received 23 June 2021; accepted 18 November 2021; published 27 December 2021)

Detecting the orientation of the Néel vector is a major research topic in antiferromagnetic spintronics. Here we recognize the intrinsic nonlinear Hall effect, which is independent of the relaxation time, as a prominent contribution to the time-reversal-odd second order conductivity and can be used to detect the reversal of the Néel vector. In contrast, the Berry-curvature-dipole-induced nonlinear Hall effect depends linearly on relaxation time and is time-reversal even. We study the intrinsic nonlinear Hall effect in an antiferromagnetic metal: tetragonal CuMnAs, and show that its nonlinear Hall conductivity can reach the order of $\mathrm{mA/V^2}$. The dependence on the chemical potential of such nonlinear Hall conductivity can be qualitatively explained by a tilted massive Dirac model. Moreover, we demonstrate its strong temperature dependence and briefly discuss its competition with the second order Drude conductivity. Finally, a complete survey of magnetic point groups is presented, providing guidelines for finding more antiferromagnetic materials with the intrinsic nonlinear Hall effect.

DOI: 10.1103/PhysRevLett.127.277201

Introduction.—Electrically detecting the reversal (180° rotation) of the Néel vector is a crucial task in antiferromagnetic spintronics [1,2]. Since the Néel vector and its reversed image are related by time reversal symmetry, the time-reversal-odd (T-odd) part of the conductivity tensor can be utilized to distinguish them. However, many antiferromagnets respect the combination of spatial and time reversal symmetry (PT), which forbids the T-odd part of the linear conductivity tensor. In contrast, for the second order conductivity tensor, PT symmetry forbids the time-reversal-even (T-even) part and allows the existence of the T-odd part. Therefore, second order conductivity is an ideal quantity to detect the Néel vector reversal in PT-symmetric antiferromagnets. In fact, one pioneering experiment detected the Néel vector reversal by measuring the sign of the second order conductivity in antiferromagnetic tetragonal CuMnAs [3]. Despite the success of the experiment, the underlying microscopic mechanism of this second order conductivity has not been fully recognized.

The second order conductivity tensor is defined as the quadratic current response $\boldsymbol{J}$ to electric field $\boldsymbol{E}$: $J^\alpha = \sum_{\beta,\gamma} \sigma^{\alpha\beta\gamma} E^\beta E^\gamma$ (α, β, and γ are Cartesian indices). σ can be separated into an Ohmic-type part and a Hall-type part [4]. The Ohmic part includes a second-order Drude conductivity, which is T-odd and quadratically dependent on the relaxation time τ [5–8]. The Hall part also includes a T-odd contribution which is independent of the relaxation time, and is therefore called the intrinsic nonlinear Hall effect (INHE) [9]. The INHE is different from the more well-known Berry curvature dipole (BCD) contribution [10–14]. The latter is proportional to τ and, more importantly, it is a T-even quantity and is forbidden in PT-symmetric antiferromagnets. The INHE and its thermal counterpart, the intrinsic nonlinear Nernst effect, has been studied in model Hamiltonians such as the loop current model [15]. However, little is known about the INHE in realistic materials.

In this Letter, we show that the INHE is a prominent contribution, and sometimes the dominant contribution, to the T-odd second order conductivity. Using density functional theory (DFT) calculations, we show that σ_{INH} in antiferromagnetic tetragonal CuMnAs can reach the order of $\mathrm{mA/V^2}$ and is much larger than the Ohmic second order Drude conductivity. We find a large peak accompanied by a sign change of σ_{INH} as a function of the chemical potential. This behavior can be explained by a tilted massive Dirac fermion model in which the INHE is shown to have a geometric origin arising from the quantum metric dipole. We find that σ_{INH} in tetragonal CuMnAs has a strong temperature dependence and briefly discuss its competition with second order Drude conductivity. Finally, a complete survey of magnetic point groups is presented, providing guidelines for finding other candidate materials where the INHE can be observed. Our results thus establish the INHE as an important transport phenomena in inversion asymmetric magnetic metals, particularly in the context of probing the Néel vector reversal in antiferromagnets.

Intrinsic nonlinear Hall effect in CuMnAs.—CuMnAs usually crystallizes in an orthorhombic phase. However, with a suitable substrate (e.g., GaAs or GaP), a tetragonal

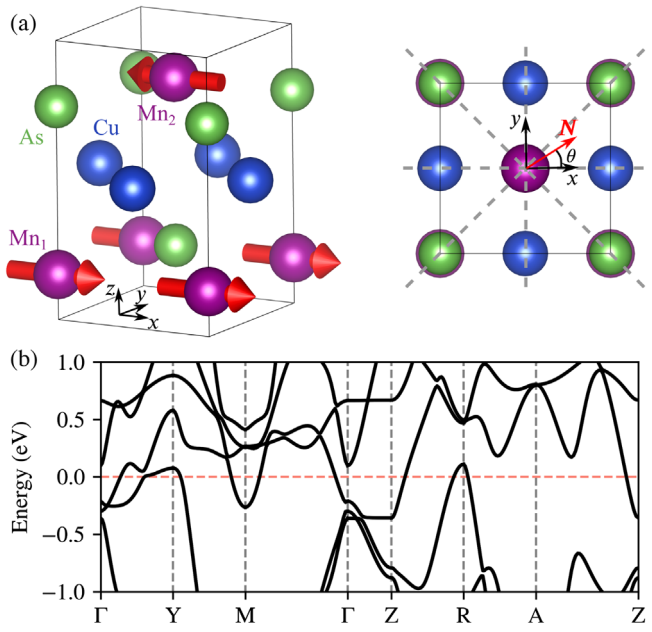

FIG. 1. (a) The unit cell of tetragonal CuMnAs (left) and its top view (right). Mn_1 and Mn_2 have opposite magnetic moments, both lying in the x-y plane. Important crystalline symmetries without magnetic order include inversion (inversion center between Mn_1 and Mn_2 on the left panel), fourfold rotation in the z direction (rotation axis at the Mn atom in the right panel), and four mirror symmetries (mirror planes indicated by dashed gray lines in the right panel). The Néel vector $\boldsymbol{N}$ is parametrized by the polar angle θ in the x-y plane. (b) The band structure of CuMnAs for $\theta = 0$.

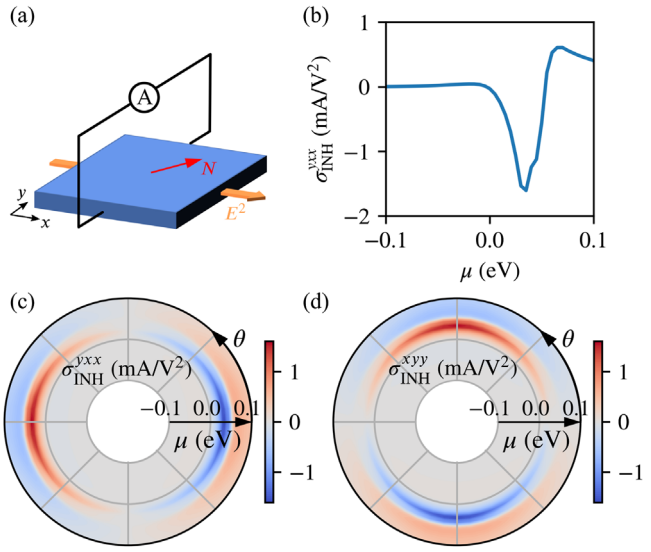

FIG. 2. (a) A sketch of the experimental setup to measure σ^{yxx}. The x and y directions are defined in Fig. 1. (b) $\sigma^{yxx}_{\mathrm{INH}}$ for $\theta = 0$ as a function of the chemical potential. (c)–(d) Intrinsic nonlinear Hall conductivity $\sigma^{yxx}_{\mathrm{INH}}$ [(c)] and $\sigma^{xyy}_{\mathrm{INH}}$ [(d)] as a function of chemical potential (μ) and orientation of the Néel vector θ. $\mu = 0$ is the intrinsic chemical potential.

phase can be experimentally grown [16], which is the focus of this work. Figure 1(a) presents the atomic structure and important symmetries of tetragonal CuMnAs. Each unit cell contains two Mn planes. The magnetic moment, lying in the Mn plane, is antiferromagnetically ordered between the planes. For magnetic moments lying in different directions within the Mn plane, there is little energy difference. Therefore, the Néel vector $\boldsymbol{N}$, defined as the difference of the magnetic moments between Mn_1 and Mn_2 atoms, can be parametrized by the polar angle θ [see Fig. 1(a)]. For arbitrary θ, PT symmetry is respected. Electrical manipulation of θ using current pulses has recently been demonstrated [17,18].

The intrinsic nonlinear Hall conductivity can be expressed in terms of band quantities as [9,15]

$$\sigma^{\alpha\beta\gamma}_{\mathrm{INH}} = 2e^3 \sum_{n,m}^{\epsilon_n \neq \epsilon_m} \mathrm{Re} \int \frac{d^3\boldsymbol{k}}{(2\pi)^3} \frac{v^\alpha_n A^\beta_{nm} A^\gamma_{mn}}{\epsilon_n - \epsilon_m} \frac{\partial f(\epsilon_n)}{\partial \epsilon_n} - (\alpha \leftrightarrow \beta), \tag{1}$$

where $\boldsymbol{v}$ is the band velocity, ϵ_n is the energy of the nth Bloch state, $\boldsymbol{A}_{nm} = \langle u_n | i\nabla_{\boldsymbol{k}} u_m \rangle$ is the Berry connection with $|u_n\rangle$ the periodic part of the nth Bloch state, and e is the (positive) elementary charge. $f(\epsilon; T, \mu)$ [T and μ are omitted in Eq. (1)] is the Fermi-Dirac occupation number for energy ϵ at temperature T and chemical potential μ. For now we work at $T = 0$. We note that $\sigma^{\alpha\beta\gamma}_{\mathrm{INH}}$ is antisymmetric with respect to α and β, therefore it describes a Hall-type current [4]. Because of the derivative of f in Eq. (1), the INHE only depends on quantities around the Fermi surface and is only relevant for metals. As shown in Fig. 1(b), CuMnAs is indeed a metal.

For a general orientation (not along high symmetric directions such as $\theta = 0$) of the Néel vector, the magnetic point group of tetragonal CuMnAs is $2'/m$. The allowed components are $\sigma^{xyy}_{\mathrm{INH}} = -\sigma^{yxy}_{\mathrm{INH}}$, $\sigma^{yxx}_{\mathrm{INH}} = -\sigma^{xyx}_{\mathrm{INH}}$, $\sigma^{xzz}_{\mathrm{INH}} = -\sigma^{zxz}_{\mathrm{INH}}$, and $\sigma^{yzz}_{\mathrm{INH}} = -\sigma^{zyz}_{\mathrm{INH}}$. Fourfold rotational symmetry along the z axis (C_{4z}) demands that $\sigma^{xyy(xzz)}_{\mathrm{INH}}(\theta) = \sigma^{yxx(yzz)}_{\mathrm{INH}}(\theta + \pi/2)$. Therefore, the only independent components are $\sigma^{yxx}_{\mathrm{INH}}$ and $\sigma^{yzz}_{\mathrm{INH}}$. Here we focus on $\sigma^{yxx}_{\mathrm{INH}}$ and defer the discussion of $\sigma^{yzz}_{\mathrm{INH}}$ to the Supplemental Material [19].

We first examine the chemical potential (μ) dependence of $\sigma^{yxx}_{\mathrm{INH}}$. A sketch of the experimental setup to measure σ^{yxx} is presented in Fig. 2(a). When the Néel vector is along the x axis ($\theta = 0$), $\sigma^{yxx}_{\mathrm{INH}}$ is generally small for hole doping, but develops a peak and then changes sign rapidly and develops another peak for electron doping [Fig. 2(b)]. This behavior signifies a strong variation of Bloch wave function in the band structure, and will be discussed later. As shown in Fig. 2(b), $\sigma^{yxx}_{\mathrm{INH}}$ is on the order of $\mathrm{mA/V^2}$.

Next, we discuss the strong correlation between σ_{INH} and the orientation of the Néel vector [Figs. 2(c)–2(d)]. In most cases, symmetry arguments can be invoked to explain the correlation. As mentioned in the introduction, time reversal

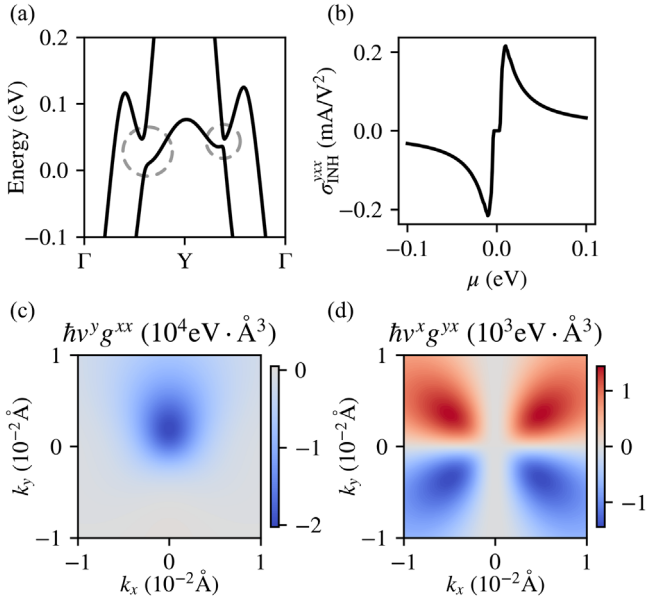

FIG. 3. (a) The band structure of tetragonal CuMnAs along the Γ-Y-Γ line, which contains two avoided crossings. (b) The intrinsic nonlinear Hall conductivity of a tilted massive Dirac model. (c) and (d) The quantum metric tensor dipole at the $k_z = 0$ plane for the lower band. $\hbar$ is the reduced Planck constant. Parameters: $t = 0.8$ eV/Å, $m = 5$ meV.

symmetry demands $\sigma_{\mathrm{INH}}(\theta) = -\sigma_{\mathrm{INH}}(\theta + \pi)$. Additional constraints on specific components can be derived from crystalline symmetries. For example, when the Néel vector is along the x (y) direction, $\sigma_{\mathrm{INH}}^{xyy}$ ($\sigma_{\mathrm{INH}}^{yxx}$) is forbidden by mirror symmetry in the x (y) direction. Therefore, the sign of $\sigma_{\mathrm{INH}}^{yxx}$ can be used to distinguish the Néel vector lying in $\pm x$ direction [Fig. 2(c)], and the sign of $\sigma_{\mathrm{INH}}^{xyy}$ can be used to distinguish the Néel vector lying in $\pm y$ direction [Fig. 2(d)].

Tilted massive Dirac point model.—To gain further insight into the behavior of $\sigma_{\mathrm{INH}}^{yxx}$, we analyze the contribution to $\sigma_{\mathrm{INH}}^{yxx}$ from different k points at the Fermi surface. We find that the dominant contribution of the peak comes from avoided crossings along the Γ-X-Γ and Γ-Y-Γ lines. Figure 3(a) shows the band structure along the Γ-Y-Γ line, where two avoided crossings can be observed. These avoided crossings are common on these high symmetry lines since the little groups on these lines have only one allowed representation.

These avoided crossings can be qualitatively modeled by tilted massive Dirac points. Specifically, we introduce the following Hamiltonian:

$$H_{\mathrm{Dirac}} = k_x \tau_1 \sigma_0 + k_y(\tau_2 \sigma_2 - t\tau_0 \sigma_0) + k_z \tau_3 \sigma_0 + m\tau_2 \sigma_3, \quad (2)$$

where τ and σ are two sets of Pauli matrices, t is a parameter controlling the tilt of the Dirac point, and m controls the gap. H_{Dirac} respects the PT symmetry, which is represented by $-i\sigma_2 K$, with K the complex conjugate. Therefore, every band is doubly degenerate.

σ_{INH} is expected to have a large value if the chemical potential is near the band edge. As the chemical potential approaches the band edge, the carrier density decreases. However, the Bloch function is rapidly changing, giving rise to a large Berry connection [cf. Eq. (1)]. Because of such competition, σ_{INH} is zero when the chemical potential is right at the band edge and rapidly develops a peak before decreasing as the chemical potential moves away from the band edge. Indeed, two peaks with opposite signs can be found in $\sigma_{\mathrm{INH}}^{yxx}$ as a function of chemical potential [Fig. 3(b)], mimicking the sign change in Fig. 2(c). The tilt of the Dirac point is essential for the INHE: without the tilt in the y direction, this model has inversion symmetry, which forbids all components of second order conductivity. This calculation qualitatively explains $\sigma_{\mathrm{INH}}^{yxx}$ in CuMnAs and shows that a large INHE should be generally expected for materials with similar band structures.

Using H_{Dirac}, we find that σ_{INH} has a geometric origin as it is related to the quantum metric dipole. We use νi to label different bands, with $\nu = 1, 2$ for different sets of bands and $i = 1, 2$ for the PT-related degenerate pair. Then Eq. (1) becomes [19]

$$\sigma_{\mathrm{INH}}^{\alpha\beta\gamma} = 2e^3 \sum_{\nu} \int \frac{d^3\boldsymbol{k}}{(2\pi)^3} \frac{v_\nu^\alpha g_\nu^{\beta\gamma}}{\epsilon_\nu - \epsilon_{\bar{\nu}}} \frac{\partial f(\epsilon_\nu)}{\partial \epsilon_\nu} - (\alpha \leftrightarrow \beta), \quad (3)$$

with $\bar{\nu} \neq \nu$. The quantum metric tensor $g_\nu^{\alpha\beta}$ measures the distance between neighbouring Bloch states, and is defined as $g_\nu^{\alpha\beta} = \sum_{ij} \mathrm{Re}[A_{\nu i,\bar{\nu} j}^\alpha A_{\bar{\nu} j,\nu i}^\beta]$, with $\bar{\nu} \neq \nu$. $v_\nu^\alpha g_\nu^{\alpha\beta}$ can be regarded as the quantum metric tensor dipole. For $\sigma_{\mathrm{INH}}^{yxx}$, the two relevant quantum metric dipoles are $v_\nu^y g_\nu^{xx}$ and $v_\nu^x g_\nu^{yx}$, which are plotted for the lower band in Figs. 3(c),3(d). $\sigma_{\mathrm{INH}}^{yxx}$ is determined by the difference between these two dipoles, and hence nonzero as observed from the figure.

In some antiferromagnets, massless Dirac points can also be realized with certain crystalline symmetries [26–28]. For massless Dirac points with $m \to 0$ in Eq. (2), the expression of σ_{INH} [Eq. (1)] diverges when the chemical potential lies exactly at the Dirac point. Disorder is the most likely source that will regularize the behavior of second order conductivity for band touchings, and further theoretical investigation is needed.

Temperature dependence.—By multiplying Eq. (1) with $\int d\lambda \delta(\epsilon_n - \lambda)$, the INHE at finite temperatures can be expressed as a weighted integration of the INHE at zero temperature around the chemical potential μ as $\sigma_{\mathrm{INH}}(T, \mu) = \int d\lambda \sigma_{\mathrm{INH}}(T = 0, \lambda)[-\partial f(\lambda; T, \mu)/\partial\lambda]$. Finite temperature modifies σ_{INH} in two ways: T directly enters the Fermi-Dirac distribution and μ has a small dependence on temperature.

Assuming finite electron density, we calculate the dependence of chemical potential on T. μ decreases

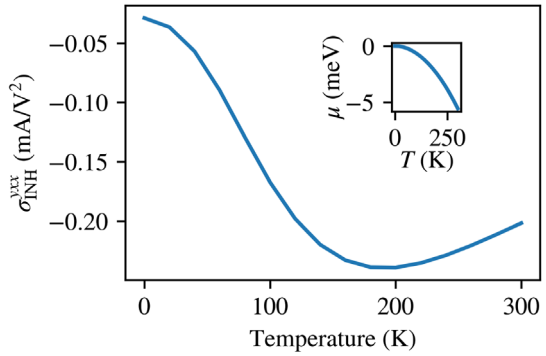

FIG. 4. The temperature dependence of intrinsic nonlinear Hall conductivity in tetragonal CuMnAs. Inset: temperature dependence of the chemical potential calculated with the assumption of constant electron density.

quadratically with respect to T, as expected from the Sommerfeld expansion. At room temperature, μ drops by 5 meV. Figure 4 shows the behavior of $\sigma_{\rm INH}$ as a function of T, where both $\sigma^{yxx}_{\rm INH}$ and $\sigma^{yzz}_{\rm INH}$ have a strong dependence on temperature. Especially, $\sigma^{yxx}_{\rm INH}$ receives an order of magnitude enhancement near room temperature. We find that this drastic change comes from the broadening of $-\partial f(\lambda;T,\mu)/\partial\lambda$, which can take advantage of the large INHE away from the intrinsic chemical potential; the change of μ plays a negligible role in the temperature dependence of $\sigma_{\rm INH}$.

Second order Drude conductivity.—$\sigma_{\rm INH}$ is not the only member of T-odd second order conductivity. Especially, the Drude conductivity can also be generalized to second order as [5–8]

$$\sigma^{\alpha\beta\gamma}_{\rm Drude} = -\frac{e^3\tau^2}{\hbar^3}\sum_n \int \frac{d^3\boldsymbol{k}}{(2\pi)^3}(\partial_{k^\alpha}\partial_{k^\beta}\partial_{k^\gamma}\epsilon_n)f(\epsilon_n). \quad (4)$$

$\sigma^{\alpha\beta\gamma}_{\rm Drude}$ is also a Fermi surface property, because an integration by parts can bring the k derivative to $f(\epsilon_n)$. In contrast to the INHE, $\sigma^{\alpha\beta\gamma}_{\rm Drude}$ only depends on the band dispersion and is symmetric with respect to the permutation of all its Cartesian indices. Since $\sigma_{\rm Drude}$ is proportional to τ^2, it also requires time reversal symmetry breaking and is allowed by PT symmetry. In moderately conducting samples, $\sigma_{\rm INH}$ is expected to dominate over $\sigma_{\rm Drude}$. Our estimation indeed shows that $\sigma_{\rm Drude}$ is only a fraction of $\sigma_{\rm INH}$ for tetragonal CuMnAs at room temperature at the intrinsic Fermi energy [19].

Magnetic point groups for INHE observation.—Tetragonal CuMnAs is only one example where the INHE is prominent. To find other materials candidates, symmetry guidelines are needed. Symmetry groups that forbid $\sigma_{\rm BCD}$ but not $\sigma_{\rm INH}$ can be found based on the fact that they transform oppositely under time reversal operation. $\sigma_{\rm Drude}$ can be distinguished from $\sigma_{\rm INH}$ and $\sigma_{\rm BCD}$ by noticing $\sigma_{\rm Drude}$ transforms as a symmetric rank-3 tensor while both $\sigma_{\rm BCD}$ and $\sigma_{\rm INH}$ transform as rank-2 pseudo-tensors under point-group operations. For example, C_{4z} constrains second order conductivity as $\sigma^{xyz} = -\sigma^{yxz}$, which is compatible with $\sigma_{\rm INH}$ and $\sigma_{\rm BCD}$ but not $\sigma_{\rm Drude}$.

TABLE I. Magnetic point groups classified by the existence or absence of INHE, second order Drude conductivity and BCD-induced NHE. For a second order conductivity tensor $\sigma^{\alpha\beta\gamma}$, only the $\beta \leftrightarrow \gamma$ permutation symmetric part contributes to the current. Therefore, in Table I, we have an extra constraint that such symmetric part does not vanish.

Magnetic point groups	INHE	Drude	BCD
$4/m'm'm'$, $-6'm'2$, $6/m'm'm'$	✓	✗	✗
-6, $6'/m$, $-6m2$, $-6m'2'$, $6'/mmm'$, 23, $m'-3'$, $4'32'$, $-43m$, $m'-3'm$	✗	✓	✗
$11'$, $21'$, $m1'$, $2221'$, $mm21'$, $41'$, $-41'$, $4221'$, $4mm1'$, $-42m1'$, $31'$, $321'$, $3m1'$, $61'$, $6221'$, $6mm1'$	✗	✗	✓
$-1'$, $2'/m$, $2/m'$, $m'mm$, $m'm'm'$, $4/m'$, $4'/m'$, $4/m'mm$, $4'/m'm'm$, $-3'$,$-3'm$, $-3'm'$, $-6'$, $6/m'$, $-6'm2'$, $6/m'mm$	✓	✓	✗
422, $4m'm'$, $-4'2m'$, 622, $6m'm'$	✓	✗	✓
$6'$, $6'22'$, $6'mm'$	✗	✓	✓
$1,2$, $2'$, m, m', 222, $2'2'2$, $mm2$, $m'm2'$, $m'm'2$, 4, $4'$, -4, $-4'$, $4'22'$, $42'2'$, $4mm$, $4'm'm$, $-42m$, $-4'2'm$, $-42'm'$, 3, 32, $32'$, $3m$, $3m'$, 6, $62'2'$, $6mm$	✓	✓	✓

Table I presents a classification of magnetic point groups according to the existence or absence of the INHE, second order Drude conductivity, and BCD contribution. There are indeed three magnetic point groups where the INHE is allowed but second order Drude conductivity and BCD contribution are forbidden (first row of Table I). For the three groups, the allowed $\sigma_{\rm INH}$ components are of the type $\sigma^{xyz}_{\rm INH}$. More magnetic point groups can be included if we allow for the existence of second order Drude conductivity. 16 magnetic point groups belong to this class (fourth row of Table I), which includes $2'/m$, the magnetic point group of tetragonal CuMnAs. Out of all 122 magnetic point groups, 53 allows INHE (Table I). Some of the groups allow both INHE and BCD contribution, enabling the comparison between these two contributions.

There are also magnetic point groups that allow BCD contribution but forbid INHE (third and sixth row of Table I), most of which contain time reversal symmetry. It is worth noting that some antiferromagnetic materials actually belong to these magnetic point groups. For example, antiferromagnetic cubic CuMnSb breaks the inversion symmetry but respects the combination of time reversal and translation symmetry, and the corresponding

magnetic point group will have time reversal as a symmetry element. As a result, both the INHE and the second order Drude contribution are forbidden, but BCD contribution is allowed and can be used to detect the 90° (but not 180°) reorientation of the Néel vector [29].

Discussion and summary.—In a recent experiment on tetragonal CuMnAs, the second order conductivity has been measured [3]. While the dependence of the conductivity on the rotation angle of the Néel vector agrees with our symmetry analysis, the experimental value is at least 1 order of magnitude smaller than our calculation. Several factors could play a role here, including the highly sensitive doping and temperature dependence of the INHE and the existence of antiferromagnetic domains [30–32]. More investigations are needed for a quantitative comparison between our theory and the experiment.

Beyond isotropic relaxation approximation, skew scattering and side jump arising from disorder effects also contribute to the second-order conductivity, but INHE remains the only contribution that is independent of the relaxation time. Extensive efforts [33–39] have been put into disorder-induced NHE in time reversal symmetric systems. The behavior of these contributions in magnetic systems and their role in possible spintronics applications remains to be explored.

In summary, we have shown that the INHE leads to a dominant contribution to the second order conductivity in tetragonal CuMnAs. More importantly, we find that the INHE can not only reflect the microscopic geometric properties of Bloch electrons, but also respond sensitively to the orientation of the Néel vector, providing a promising way to detect the reversal of the Néel vector. Our symmetry analysis shows that the INHE is widely available and hence should be recognized as a fundamental transport phenomenon in antiferromagnetic spintronics.

We acknowledge stimulating discussions with T. Jungwirth, D. C. Ralph, and J. Železný. This work is supported by AFOSR MURI 2D MAGIC (FA9550-19-1-0390). Y. G. also acknowledges support from the Startup Foundation from USTC. This work used the Extreme Science and Engineering Discovery Environment (XSEDE), which is supported by National Science Foundation Grant No. ACI-1548562. Specifically, it used the Bridges-2 system, which is supported by NSF Grant No. ACI-1928147, at the Pittsburgh Supercomputing Center (PSC).

Note added in the proof.—During the refereeing process, we became aware of another paper calculating INHE of Mn_2Au [40].

*ygao87@ustc.edu.cn
†dixiao@uw.edu

[1] T. Jungwirth, X. Marti, P. Wadley, and J. Wunderlich, Antiferromagnetic spintronics, Nat. Nanotechnol. **11**, 231 (2016).
[2] V. Baltz, A. Manchon, M. Tsoi, T. Moriyama, T. Ono, and Y. Tserkovnyak, Antiferromagnetic spintronics, Rev. Mod. Phys. **90**, 015005 (2018).
[3] J. Godinho, H. Reichlová, D. Kriegner, V. Novák, K. Olejník, Z. Kašpar, Z. Šobáň, P. Wadley, R. P. Campion, R. M. Otxoa, P. E. Roy, J. Železný, T. Jungwirth, and J. Wunderlich, Electrically induced and detected Néel vector reversal in a collinear antiferromagnet, Nat. Commun. **9**, 4686 (2018).
[4] S. S. Tsirkin and I. Souza, On the separation of Hall and Ohmic nonlinear responses, arXiv:2106.06522.
[5] T. Holder, D. Kaplan, and B. Yan, Consequences of time-reversal-symmetry breaking in the light-matter interaction: Berry curvature, quantum metric, and diabatic motion, Phys. Rev. Research **2**, 033100 (2020).
[6] H. Watanabe and Y. Yanase, Nonlinear electric transport in odd-parity magnetic multipole systems: Application to mn-based compounds, Phys. Rev. Research **2**, 043081 (2020).
[7] H. Watanabe and Y. Yanase, Chiral Photocurrent in Parity-Violating Magnet and Enhanced Response in Topological Antiferromagnet, Phys. Rev. X **11**, 011001 (2021).
[8] J. Železný, Z. Fang, K. Olejník, J. Patchett, F. Gerhard, C. Gould, L. W. Molenkamp, C. Gomez-Olivella, J. Zemen, T. Tichý, T. Jungwirth, and C. Ciccarelli, Unidirectional magnetoresistance and spin-orbit torque in nimnsb, Phys. Rev. B **104**, 054429 (2021).
[9] Y. Gao, S. A. Yang, and Q. Niu, Field Induced Positional Shift of Bloch Electrons and Its Dynamical Implications, Phys. Rev. Lett. **112**, 166601 (2014).
[10] I. Sodemann and L. Fu, Quantum Nonlinear Hall Effect Induced by Berry Curvature Dipole in Time-Reversal Invariant Materials, Phys. Rev. Lett. **115**, 216806 (2015).
[11] E. Deyo, L. Golub, E. Ivchenko, and B. Spivak, Semiclassical theory of the photogalvanic effect in non-centrosymmetric systems, arXiv:0904.1917.
[12] J. E. Moore and J. Orenstein, Confinement-Induced Berry Phase and Helicity-Dependent Photocurrents, Phys. Rev. Lett. **105**, 026805 (2010).
[13] Q. Ma *et al.*, Observation of the nonlinear Hall effect under time-reversal-symmetric conditions, Nature (London) **565**, 337 (2019).
[14] K. Kang, T. Li, E. Sohn, J. Shan, and K. F. Mak, Nonlinear anomalous hall effect in few-layer WTe2, Nat. Mater. **18**, 324 (2019).
[15] Y. Gao and D. Xiao, Orbital magnetic quadrupole moment and nonlinear anomalous thermoelectric transport, Phys. Rev. B **98**, 060402(R) (2018).
[16] P. Wadley *et al.*, Tetragonal phase of epitaxial room-temperature antiferromagnet CuMnAs, Nat. Commun. **4**, 2322 (2013).
[17] P. Wadley *et al.*, Electrical switching of an antiferromagnet, Science **351**, 587 (2016).
[18] P. Wadley, S. Reimers, M. J. Grzybowski, C. Andrews, M. Wang, J. S. Chauhan, B. L. Gallagher, R. P. Campion, K. W. Edmonds, S. S. Dhesi, F. Maccherozzi, V. Novak, J. Wunderlich, and T. Jungwirth, Current polarity-dependent manipulation of antiferromagnetic domains, Nat. Nanotechnol. **13**, 362 (2018).
[19] See Supplemental Material at http://link.aps.org/supplemental/10.1103/PhysRevLett.127.277201 containing

DFT calculation methods, the *yzz* component of INHE, second order Drude conductivity, and the relation between INHE and the geometric tensor. The Supplemental Material cites Refs. [20–25].

[20] G. Kresse and J. Furthmüller, Efficient iterative schemes for *ab initio* total-energy calculations using a plane-wave basis set, Phys. Rev. B **54**, 11169 (1996).

[21] G. Kresse and D. Joubert, From ultrasoft pseudopotentials to the projector augmented-wave method, Phys. Rev. B **59**, 1758 (1999).

[22] G. Pizzi *et al.*, Wannier90 as a community code: New features and applications, J. Phys. Condens. Matter **32**, 165902 (2020).

[23] P. E. Blöchl, Projector augmented-wave method, Phys. Rev. B **50**, 17953 (1994).

[24] J. P. Perdew, K. Burke, and M. Ernzerhof, Generalized Gradient Approximation Made Simple, Phys. Rev. Lett. **77**, 3865 (1996).

[25] M. Veis *et al.*, Band structure of CuMnAs probed by optical and photoemission spectroscopy, Phys. Rev. B **97**, 125109 (2018).

[26] P. Tang, Q. Zhou, G. Xu, and S.-C. Zhang, Dirac fermions in an antiferromagnetic semimetal, Nat. Phys. **12**, 1100 (2016).

[27] D.-F. Shao, G. Gurung, S.-H. Zhang, and E. Y. Tsymbal, Dirac Nodal Line Metal for Topological Antiferromagnetic Spintronics, Phys. Rev. Lett. **122**, 077203 (2019).

[28] L. Šmejkal, J. Železný, J. Sinova, and T. Jungwirth, Electric Control of Dirac Quasiparticles by Spin-Orbit Torque in an Antiferromagnet, Phys. Rev. Lett. **118**, 106402 (2017).

[29] D.-F. Shao, S.-H. Zhang, G. Gurung, W. Yang, and E. Y. Tsymbal, Nonlinear Anomalous Hall Effect for Néel Vector Detection, Phys. Rev. Lett. **124**, 067203 (2020).

[30] T. Janda *et al.*, Magneto-Seebeck microscopy of domain switching in collinear antiferromagnet CuMnAs, Phys. Rev. Mater. **4**, 094413 (2020).

[31] M. S. Wörnle, P. Welter, Z. Kašpar, K. Olejník, V. Novák, R. P. Campion, P. Wadley, T. Jungwirth, C. L. Degen, and P. Gambardella, Current-induced fragmentation of antiferromagnetic domains, arXiv:1912.05287.

[32] M. J. Grzybowski, P. Wadley, K. W. Edmonds, R. Beardsley, V. Hills, R. P. Campion, B. L. Gallagher, J. S. Chauhan, V. Novak, T. Jungwirth, F. Maccherozzi, and S. S. Dhesi, Imaging Current-Induced Switching of Antiferromagnetic Domains in CuMnAs, Phys. Rev. Lett. **118**, 057701 (2017).

[33] H. Isobe, S.-Y. Xu, and L. Fu, High-frequency rectification via chiral Bloch electrons, Sci. Adv. **6**, eaay2497 (2020).

[34] Z. Z. Du, C. M. Wang, S. Li, H.-Z. Lu, and X. C. Xie, Disorder-induced nonlinear hall effect with time-reversal symmetry, Nat. Commun. **10**, 3047 (2019).

[35] S. Nandy and I. Sodemann, Symmetry and quantum kinetics of the nonlinear hall effect, Phys. Rev. B **100**, 195117 (2019).

[36] C. Xiao, Z. Z. Du, and Q. Niu, Theory of nonlinear hall effects: Modified semiclassics from quantum kinetics, Phys. Rev. B **100**, 165422 (2019).

[37] Z. Z. Du, C. M. Wang, H.-P. Sun, H.-Z. Lu, and X. C. Xie, Quantum theory of the nonlinear hall effect, Nat. Commun. **12**, 5038 (2021).

[38] E. J. König and A. Levchenko, Quantum kinetics of anomalous and nonlinear hall effects in topological semimetals, Ann. Phys. (Amsterdam) **435**, 168492 (2021).

[39] Z. Z. Du, H.-Z. Lu, and X. C. Xie, Nonlinear Hall effects, Nat. Rev. Phys. **3**, 744 (2021).

[40] H. Liu, J. Zhao, Y.-X. Huang, W. Wu, X.-L. Sheng, C. Xiao, and S. A. Yang, following Letter, Intrinsic Second-Order Anomalous Hall Effect and its Application in Compensated Antiferromagnets, Phys. Rev. Lett. **127**, 277202 (2021).